



Original Paper

The mechanical properties of Lucaogou shale layered samples and the influence of minerals on fracture propagation

Xiu-Kuo Sun ^{a, b}, Shou-Ding Li ^{a, b, c, *}, Xiao Li ^{a, b, c}, Guan-Fang Li ^{a, b, c}, Bo Zheng ^{a, b, c}, Tian-Qiao Mao ^{a, b, c}, Jing-Yun Guo ^{a, b, c}

^a State Key Laboratory of Deep Petroleum Intelligent Exploration and Development, Institute of Geology and Geophysics, Chinese Academy of Sciences, Beijing 100029, China

^b Key Laboratory of Deep Petroleum Intelligent Exploration and Development, Institute of Geology and Geophysics, Chinese Academy of Sciences, Beijing, 100029, China

^c College of Earth and Planetary Sciences, University of Chinese Academy of Sciences, Beijing, 100049, China



ARTICLE INFO

Article history:

Received 24 June 2023

Received in revised form

11 June 2024

Accepted 9 September 2024

Available online 10 September 2024

Edited by Teng Zhu and Min Li

Keywords:

Fracture propagation

Mechanical property

Real-time micro-CT scanning

Mineral composition

Lucaogou formation

ABSTRACT

Shale oil is one of the most promising alternative unconventional energies in the world, and Lucaogou Formation shows significant exploration potential, becoming the primary target in northwestern China. This paper compared the mechanical properties of shale layered samples from oil layer and interlayer of Lucaogou Formation, using uniaxial compressive tests with real-time micro-CT scanning. After that, the mineral analysis was conducted on one cross-section of the fractured sample to analyze the influence of mineral composition and distribution on micro-crack propagation. Such research has rarely been reported before. The results showed the surface porosity and elastic modulus of oil-bearing samples is larger than that of the interlayer samples, while the uniaxial compressive strength is lower. Besides, when there is only one dominant mineral with a content greater than 60%, a main crack tends to form at this area; When there are 2–3 major minerals with a content of 10%–60%, a fractured zone with many fine micro-cracks is more likely to form here. Finally, the higher the Moh's hardness of the mineral, the more difficult it is for micro-cracks to develop through it.

© 2024 The Authors. Publishing services by Elsevier B.V. on behalf of KeAi Communications Co. Ltd. This is an open access article under the CC BY-NC-ND license (<http://creativecommons.org/licenses/by-nc-nd/4.0/>).

1. Introduction

Shale oil is one of the most important unconventional oil exploration targets at present, accounting for 20–50% of the total oil reserves across the world (Zou et al., 2012, 2013; Xu et al., 2022). The principal method to exploit shale oil is drilling and fracturing (Tulu, 2009; Chen et al., 2015; Wang et al., 2016). Unfortunately, there are still some problems need to be solved in exploitation. For example, the borehole instability is still common during drilling (Zoback et al., 1985), and the effective intervals in fracturing only account for 20–50%, with the rest intervals failing and contributing little to production (Miller et al., 2011; Wu et al., 2019). These problems are all involved with the development rules of the cracks. Since the macro-cracks are derived from the extension and inter-connection of the micro-cracks, it is important to understand how

the micro-cracks develop during the loading and the corresponding stress condition.

Many experiments have been conducted using the real-time CT scanning, in order to directly obtain the precise crack morphology corresponding to a certain stress during the fracture process. Li et al. (2017) divided the deformation and failure process of shale into six stages, successfully observed the compaction of the low-density area and the appearance of small cracks during uniaxial compression through micro-CT, and classified the failure mechanism as tension destruction and comprehensive tension-shear destruction. At different loading stages, the specific surface area correlates with fracture tortuosity, according to the geometrical characterization of fractures segmented from CT images (Zhou et al., 2018). The secondary branch cracks of rocks connected with main crack, and the propagation path for secondary ones is winding, tending to parallel to the direction of axial stress (Zhang et al., 2020).

Considering the composition of the rock itself, the mechanical parameters and fracture mode are related to the mineral type. For

* Corresponding author.

E-mail address: lsdlyh@mail.iggcas.ac.cn (S.-D. Li).

example, the elastic properties, the compacted characteristics and the frictional strength all correlate with the content of clay (Revil et al., 2002; Crawford et al., 2008; Kohli and Zoback, 2013; Sone and Zoback, 2013). By compared the clay-rich, calcareous and siliceous shale, it is found that the Young's modulus of clay-rich shale is the largest, followed by calcareous and siliceous shale; while Poisson's ratio of calcareous shale is the largest, followed by clay-rich and siliceous shale (Li et al., 2023). Li (2022) found that the Young's modulus and fracture pressure decrease significantly with rising organic matter content. Similar conclusions have been made by nanoindentation test, that an increment of Young's modulus is correlated with an increase in carbonate and quartz content, whereas, an increase in TOC, clay content and porosity decrease Young's modulus (Kumar et al., 2012; Yang et al., 2020).

Mineral compositions not only affect mechanical parameters, but also influence fracture propagation. However, such studies are relatively rare. Since different minerals own different Young's modulus and Poisson's ratio, the cracks often generate along the borders of minerals for the discontinuous stress (He et al., 2020; Li, 2022). The fracture mode in shale with low organic content typically manifests as a single shear failure, characterized by a smooth, elongated primary crack accompanied by random microcracks; As the organic matter content increases, the fractures become more complex, transitioning from simple shear fracturing to intensive splitting failure (Li, 2022). The hydraulic fractures are preferable to propagate in brittle minerals, which are tortuous with multi branches, beneficial to form hydraulic fracture network (Li et al., 2018). In addition, the predominance of small particles and/or point-point contacts are conducive to brittle failure generally, especially with high content of quartz (Li Y. et al., 2022b).

With regard to the Lucaogou Formation in Junggar Basin, it shows significant exploration potential and becomes the primary exploration target in the northwestern China (Hu et al., 2018; Luo et al., 2018). The lithology of shale oil reservoir there represents great variation in a vertical direction with bedding planes (Li J. et al., 2022a). Thus, it is fairly essential to understand the mechanical properties and fracture characteristics of different layers, which is the key to optimize the drilling and hydraulic fracturing strategy (Zhang et al., 2022).

Therefore, in this paper, the mechanical properties and the progressive fracture characteristics of shale layered samples from Lucaogou Formation were investigated, based on the uniaxial compressive tests with real-time micro-CT scanning. Specially, the samples from oil layer and interlayer were both collected, tested and compared, which has rarely been reported in previous studies. After that, the mineral analysis was conducted on the fractured samples with the ZEISS Merlin field emission scanning electron microscope (FE-SEM), and the features of micro-crack propagation with the influence of mineral composition and distribution were analyzed.

2. Material and methods

2.1. Sample preparation

The shale layered samples for this experiment were from the downhole, belonging to Lucaogou Formation in Jimsar Sag Area in the southern margin of Junggar Basin, China. Cylindrical samples were cored from 3 different rock blocks, using a hollow cylindrical, rotary core bit mounted on a drill press. Two specimens were taken from adjacent positions on each block. The top and the bottom faces of these specimens were then cut and grinded, to achieve flat and parallel surfaces for testing, with a precision of 60 μm . Finally, 6 samples of 4 mm in diameter and 8 mm in height were prepared. The prepared samples and the direction of the bedding planes are

shown in Fig. 1((a) and (b)), and the Sample Numbers are shown in Table 1. In particular, according to the logging results, the samples of Block 1 and 3 belongs to interlayers with relatively low oil content, while those for Block 2 belongs to oil layer with higher oil content.

After the samples were prepared, the uniaxial compressive tests and mineral analysis were proceeded in turn. This means that the mineral analysis was conducted on fractured samples. According to the fracture pattern, a section parallel to the end face with a relatively large area was selected (Fig. 1(c)–(d)). Mechanical polishing and argon-ion-milling were then carried out on the cut section of the sample for the next mineral analysis.

2.2. Testing devices

As described before, the experiments in this research contains two stages: The first stage is the uniaxial compression test with real-time micro-CT scanning, aiming at studying the progressive fracture features and mechanical properties of shale layered samples; The second stage is the mineral analysis, focusing on the relationship between the cracks and the mineral composition and distribution. This means two advanced experiment systems were used, and both of them were placed at the Institute of Geology and Geophysics, Chinese Academy of Sciences.

The CT equipment used in this test is a ZEISS Xradia Versa 520 3D X-ray microscope, commonly known as micro-CT. Different from the traditional X-ray CT, this micro-CT has a microscope-level magnification architecture that combines geometric and optical magnification (Li et al., 2017). The energy of the X-ray source ranges from 30 to 160 kV, and the highest imaging resolution can reach 0.7 μm , which is the highest among similar instruments at the micron level. The main components of micro-CT are X-ray source, in-situ loading device, and detector (Fig. 2(a)). The internally equipped in-situ uniaxial compressor (Deben MICROTTEST compression stage) collects stress and strain values at a rate of 3–10/s, with a maximum loading pressure of 5000 N and a loading rate of 0.03 mm/min. This loading apparatus was placed on the rotary table of the CT facility, so that it could rotate together when scanning. Therefore, the real-time CT scanning without unloading could be achieved by this micro-CT. In this research, the resolution of CT images is 5 $\mu\text{m}/\text{pixel}$.

The equipment used to analyze the mineral composition and distribution is the FE-SEM (Fig. 2(b)). This facility is equipped with AMICS automatic large-area mineral analysis system. The smallest identification area of mineral particle in AMICS is up to 0.5 μm^2 . In this research, the resolution of mineral analysis image is 0.586 $\mu\text{m}/\text{pixel}$. Apart from the AMICS system, the ATLAS system equipped on the FE-SEM was also used. ATLAS was able to stitch together multiple small images of a cross section of a rock sample into a high-resolution, large-area microstructural image. The highest resolution for the small image is 0.6 nm, and in this case, it reaches 20 nm.

2.3. Experiment procedures

After the 6 cylindrical specimens (4 mm in diameter and 8 mm in height) were prepared, the uniaxial compression test on micro-CT was conducted. To determine the appropriate stress for scan, the strength and damage process should be learned roughly in advance, by performing conventional uniaxial compression experiments without CT on Sample X-1 (Table 1). Afterwards, the tests were conducted on Sample X-2 with real-time CT scanning. According to the previous researches (Li et al., 2017; Sun et al., 2023), the cracks will start just before the peak stress. To maximize the observation of the crack initiation process, scanning is primarily focused before the peak strength. Rather than scanning at pre-set

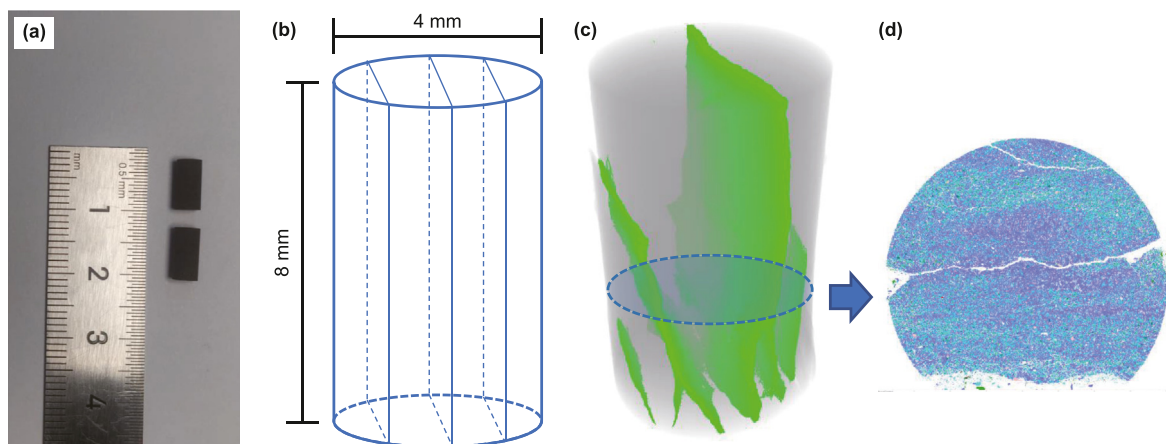


Fig. 1. (a) Two samples from one rock block; (b) The direction of the bedding planes; (c) The illustration of mineral analysis section (the green areas are cracks in the damaged sample); (d) The result of mineral analysis of the section in (c).

Table 1
The information of samples.

Sample Block	Sample Number	Oil layer /Interlayer	Experiment Item
1	1-1, 1-2	Interlayer	Sample X-1 (1-1, 2-1, 3-1):
2	2-1, 2-2	Oil layer	• Conventional uniaxial compressive test for the decision of scanning stress
3	3-1, 3-2	Interlayer	Sample X-2 (1–2, 2-2, 3-2):
			• Uniaxial compressive test with real-time micro-CT scanning
			• Mineral analysis

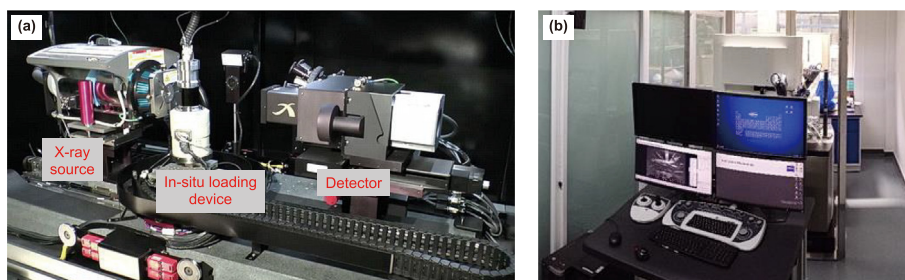


Fig. 2. (a) The ZEISS Xradia 520 Versa 3-D X-ray microscope (micro-CT); (b) The ZEISS Merlin field emission scanning electron microscope (FE-SEM).

stress levels, the scanning points were determined in real time during the uniaxial loading on Sample X-2, based on the unconfined compressive strength (UCS) and peak strain of sample X-1, as well as the fluctuations observed in the stress-strain curve during loading.

Another important aim for this research is to study the crack propagation under the influence of mineral composition and distribution. Therefore, after the CT tests, according to the fracture pattern of each sample, a section parallel to the end face with a relatively large area was selected (Fig. 1(c)–(d)), then the mineral analysis was conducted on this section by the AMICS system on FE-SEM.

In order to obtain the porosity, a square area of 1 mm × 1 mm of Sample X-2 was selected to obtain a microstructural image (Fig. 3(a)) through ATLAS system. By combining threshold segmentation and manual extraction on the stitched small images, we identified the pores (for example, the green masks in Fig. 3(b)–(c)). Calculating the total area of these pores in all the small images, and the ratio of this value to the whole area of the testing region (1 mm²) is the surface porosity.

3. Results and discussion

3.1. The progressive fracture process and mechanical features

The stress-strain curves for Sample 1–2, 2-2 and 3-2 were shown in Figs. 4–6. Before the uniaxial loading, the original state of the sample is scanned. After the loading initiates, the sample is compacted at first, where the stress presents a nonlinear rise with the increase of strain, and the slope of the curve is relatively small compared with the later stage. With the elastic deformation gradually takes the dominant position, the stress-strain curve represents linear variation. According to the previous studies (Li et al., 2017; Sun et al., 2023), cracks would not appear until the stress is getting close to the peak value. Therefore, in order to maximize the observation of the crack initiation process, the scanning points were concentrated near the peak stress. Thus, after the stress level approximately exceeds 50%, the rest scanning begins, each time taking about 25 min. During this period of time, the loading needs to be stopped, although the loading device could rotate with the rotary table on the micro-CT. This temporary pause leads to the

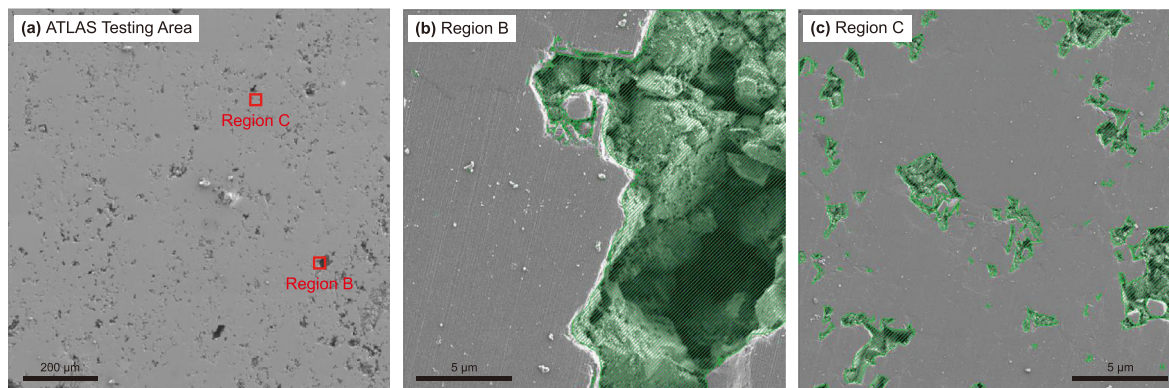


Fig. 3. (a) The microstructural image of Sample 2-1 stitched by ATLAS; (b, c) The small images with identified pores (the green masks).

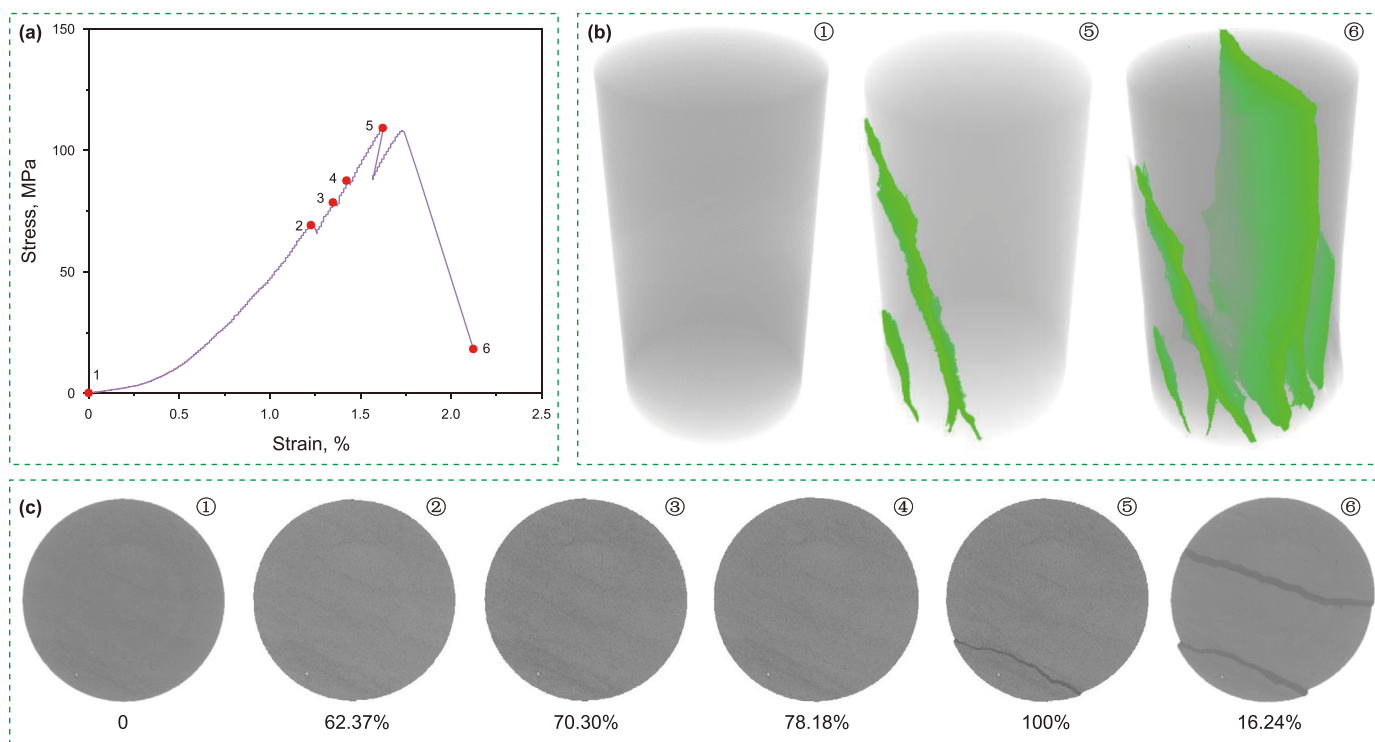


Fig. 4. The progressive fracture process of Sample 1–2. (a) The stress-strain curve with the scanning point; (b) The fracture pattern of Scanning Point 1, 5 and 6; (c) The crack propagation in the section at the sample height of 3.48 mm, with the stress level written under each image.

relaxation of the stress in the stress-strain curve. In other words, the stress will decrease a little during CT scanning. After plastic deformation occurs, the cracks start to grow. The percentage under each CT image in Figs. 4(c), 5(c) and 6(c) is the stress level at that scanning point, which is defined as the ratio of current stress to peak stress (Sun et al., 2020, 2021).

For Sample 1–2, the Scanning Point 5 is just the peak stress by coincidence, and two main cracks have appeared in the volume at this time (Fig. 4(b)). Before that, at Scanning Point 4, there are still no cracks (Fig. 4(c)). However, for Sample 2-2 and 3-2, the peak stress points were not captured. Based on the CT images, the fractures initiated at the stress level of around 91.12% and 93.39%, respectively. This shows that the stress at the time of crack emergence is very close to the peak stress, which is consistent with the previous studies. After the stress reached the peak value, the samples destroyed quickly, and the fractures developed into

complex fracture networks (Figs. 4(b), 5(b) and 6(b)).

According to the uniaxial compression test with CT scanning and the ATLAS results, the physical and mechanical parameters including surface porosity, UCS and elastic modulus (E) were calculated for the comparison of samples from interlayer and oil layer (Table 2).

Among these specimens, Sample 1-2 and 3-2 belongs to interlayer, while Sample 2-2 belongs to oil layer. The difference between the two kinds of samples is obvious in terms of surface porosity, which is much higher in Sample 2-2, nearly twice as large as that in other samples. Besides, the mechanical parameters show that the UCS for oil-bearing shale layered samples is lower than that of the interlayer ones. The distinction among UCS values is related to the surface porosity. Since the porosity is the highest in Sample 2-2, there are more weak areas in it, leading to easier fracture and lower UCS. However, the E for this sample is higher than that of the other

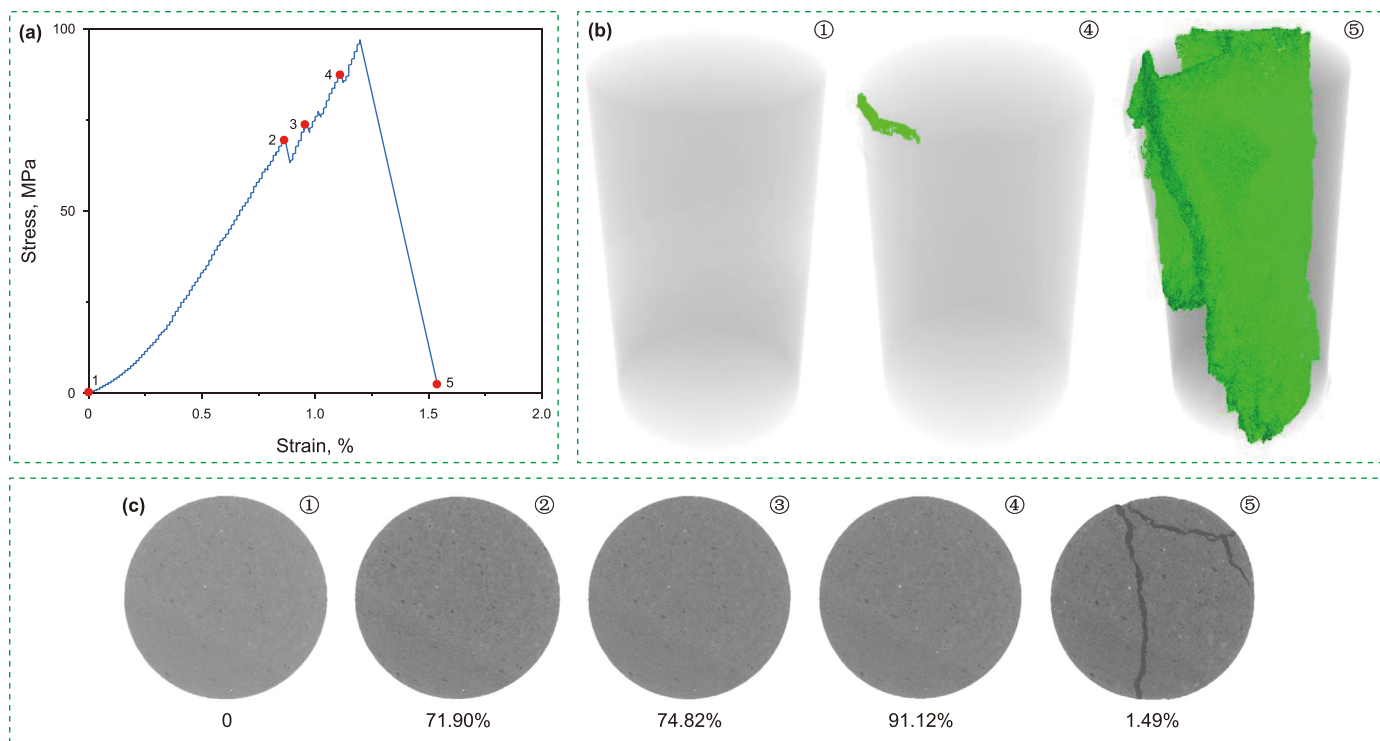


Fig. 5. The progressive fracture process of Sample 2-2. (a) The stress-strain curve with the scanning point; (b) The fracture pattern of Scanning Point 1, 4 and 5; (c) The crack propagation in the section at the sample height of 3.57 mm, with the stress level written under each image.

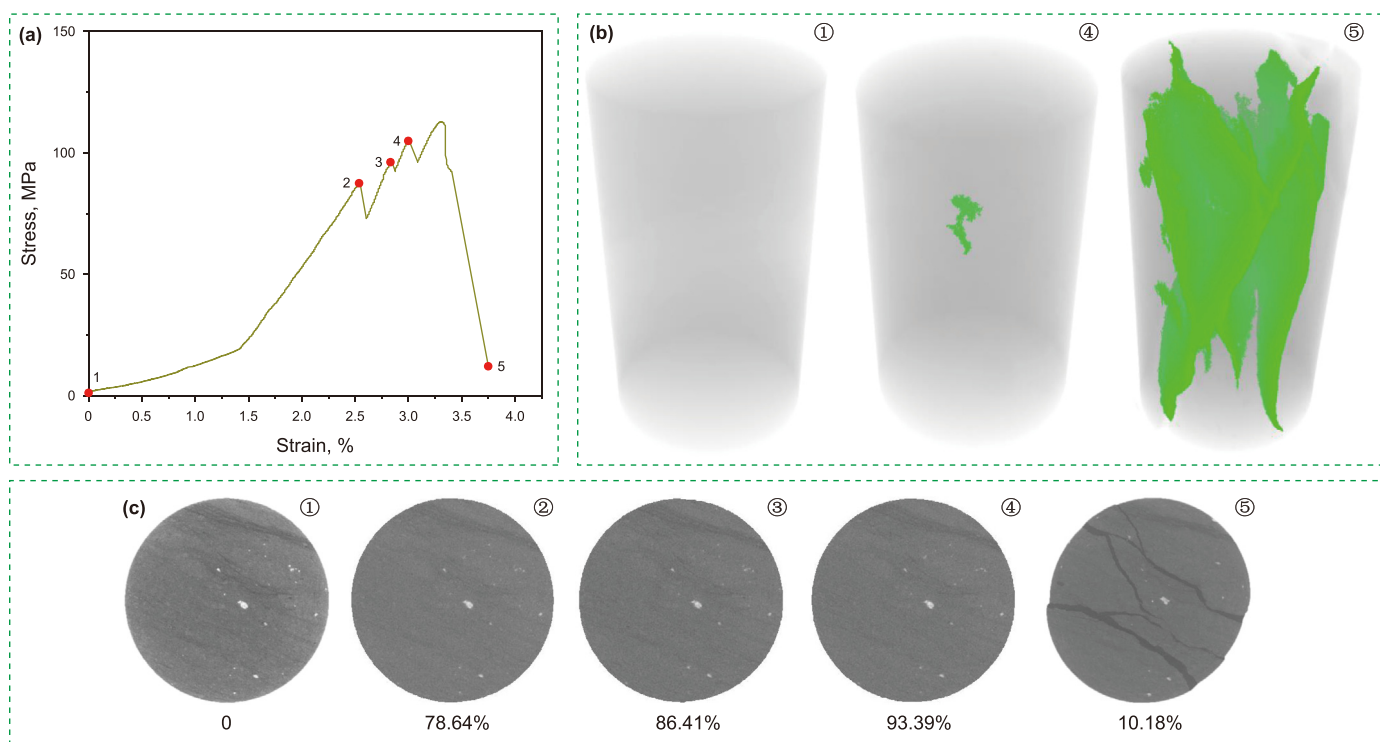


Fig. 6. The progressive fracture process of Sample 3-2. (a) The stress-strain curve with the scanning point; (b) The fracture pattern of Scanning Point 1, 4 and 5; (c) The crack propagation in the section at the sample height of 3.52 mm, with the stress level written under each image.

two samples. This may result from the mineral composition. As Section 3.2 will illustrate (Fig. 7), Sample 2-2 has a total 48.58% content of quartz and feldspar (including potassium feldspar and

albite), more than the content of 29.30% and 24.26% of Sample 1-2 and 3-2. Given the Moh's hardness 7 and 6–6.5, quartz and feldspar are both hard minerals with little deformation when loaded.

Table 2
The physical and mechanical parameters of three samples.

Sample number	Oil layer/Interlayer	Surface porosity,%	UCS, MPa	E, GPa
1-2	Interlayer	5.27	126	8.86
2-2	Oil layer	10.84	94	9.69
3-2	Interlayer	5.16	118	6.10

This may contribute to a higher *E*.

3.2. The influence of mineral composition and distribution on fracture propagation

The mineral analysis results for Sample 1-2, 2-2 and 3-2 using the AMICS automatic large-area mineral analysis system on FE-SEM are shown in Fig. 7. The first column of the figure is the backscatter selective detector (BSD) images of samples, the second column is the AMICS results of mineral composition mapping, and the third column is the mineralogical composition. Since this research mainly focuses on the influence of minerals on fracture development, the mineral analysis was conducted after sample failure. At

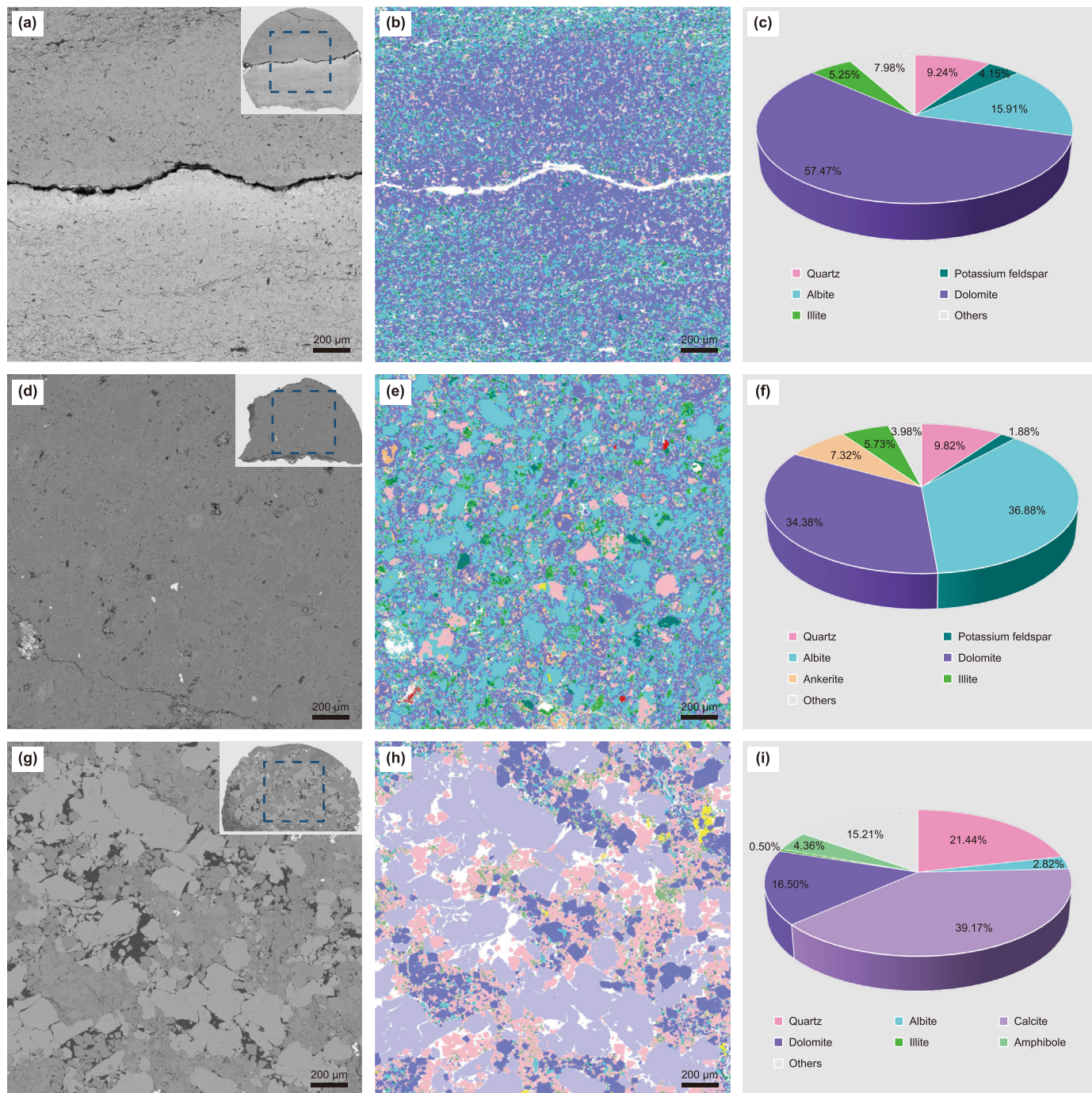


Fig. 7. The mineral analysis for three samples. (a) The backscatter selective detector (BSD) image for Sample 1-2; (b) AMICS result of mineral composition mapping for Sample 1-2; (c) Mineralogical composition for Sample 1-2; (d, e, f) are the same figures for Sample 2-2; (g, h, i) are the same figures for Sample 3-2.

this time, the sample had already broken into several pieces. Besides, in order to contain more cracks in the analysis, the field of vision is large and irregularly shaped. The resolution of the mineral analysis image is 0.586 $\mu\text{m}/\text{pixel}$.

The three testing samples are all shale layered samples, with the dolomite content of 57.47%, 34.38% and 16.50%. For Sample 1-2 and 2-2, another mineral whose content is relatively high is albite, which is 15.91% and 36.88%. As the third most abundant mineral, quartz content for the first two samples is 9.24% and 9.82%. The section of mineral analysis for Sample 3-2 happens to locate on a calcite vein, resulting in a very high calcite content of 39.17%. In addition, the quartz content reaches 21.44% in Sample 3-2, which is the highest among three samples. The clay content is similar in Sample 1-2 and 2-2 (5.25% and 5.73%), while a lot lower in Sample 3-2 (0.50%). In particular, only sample 2-2 contains ankerite, and only sample 3-2 contains amphibole.

According to the images obtained by the FE-SEM, the influence of mineral composition and distribution on fracture propagation is analyzed. The distribution of cracks and minerals in Sample 1-2 is shown in Fig. 8. There are two main cracks propagating through this section, which are in the square region B and D surrounded by the dark blue dotted line. The white color in this figure represents voids and cracks. Apart from the main cracks, there are also two main fractured veins located in Region C and E. It could be recognized that the main cracks developing in the areas where the dolomite is dominant, while the fractured veins situated in the zones where the albite and dolomite are both dispersedly distributed together. The content of minerals of Region B, C, D and E is shown in Table 3. The dolomite, as the dominant mineral in Region B and D, owns a content of more than 60%, 3.91 and 5.90 times as much as the feldspar content, which is the second abundant mineral here. This means that dolomite equals the “matrix” in these

Table 3
The area percentage of minerals and voids in different regions of Sample 1-2 (%).

	Region B	Region C	Region D	Region E
Dolomite	60.62	39.58	63.39	53.02
Feldspar	15.49	27.22	10.75	22.38
Quartz	7.25	5.72	7.43	6.47
Clay	3.68	5.89	2.95	4.18
Voids and cracks	11.85	11.78	10.67	8.93
Others	1.11	9.79	4.82	5.02

two regions. However, in Region C and E, the contents of dolomite and feldspar are much closer, being only 1.45 and 2.37 times that of feldspar, respectively. Although there are no main cracks here, the area percentage of void and crack is similar with the other two regions. This is because many fine cracks have generated here. Therefore, it could be inferred that the main cracks are more likely to develop in the area where there is one dominant mineral, whose content exceeds 60%. In addition, if two major minerals, whose contents are 10%–60%, are scattered and mixed in an area, discontinuous stress tends to form at the weak interfaces of different components, causing small fractures there. As the number of small fractures gradually increases, this area eventually forms a fractured zone.

The similar phenomenon also exists in Sample 3-2. The fractured zones are formed in the areas with different minerals scattering and mixing (Fig. 9), for example, Region B, C and D. The major mineral content is shown in Table 4. The difference is that there are three major minerals in Region B and C, including dolomite, albite and quartz. While in Region D there are only two kinds of major minerals, which are dolomite and quartz.

In Sample 2-2, there is a long thin crack with a width of 5.82 μm

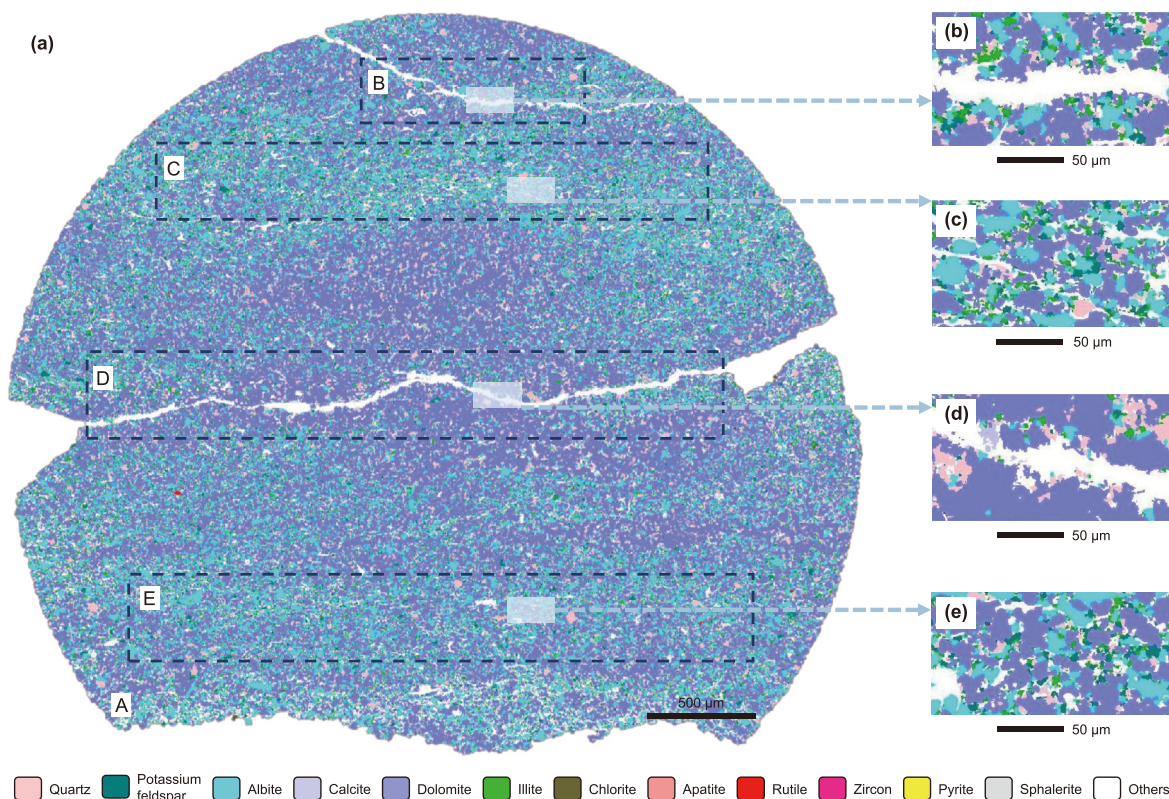


Fig. 8. The mineral composition for Sample 1-2. (a) The mineral composition mapping for the whole fractured cross-section A; (b, c, d, e) The distributions of cracks and minerals for the specific Region B, C, D, E.

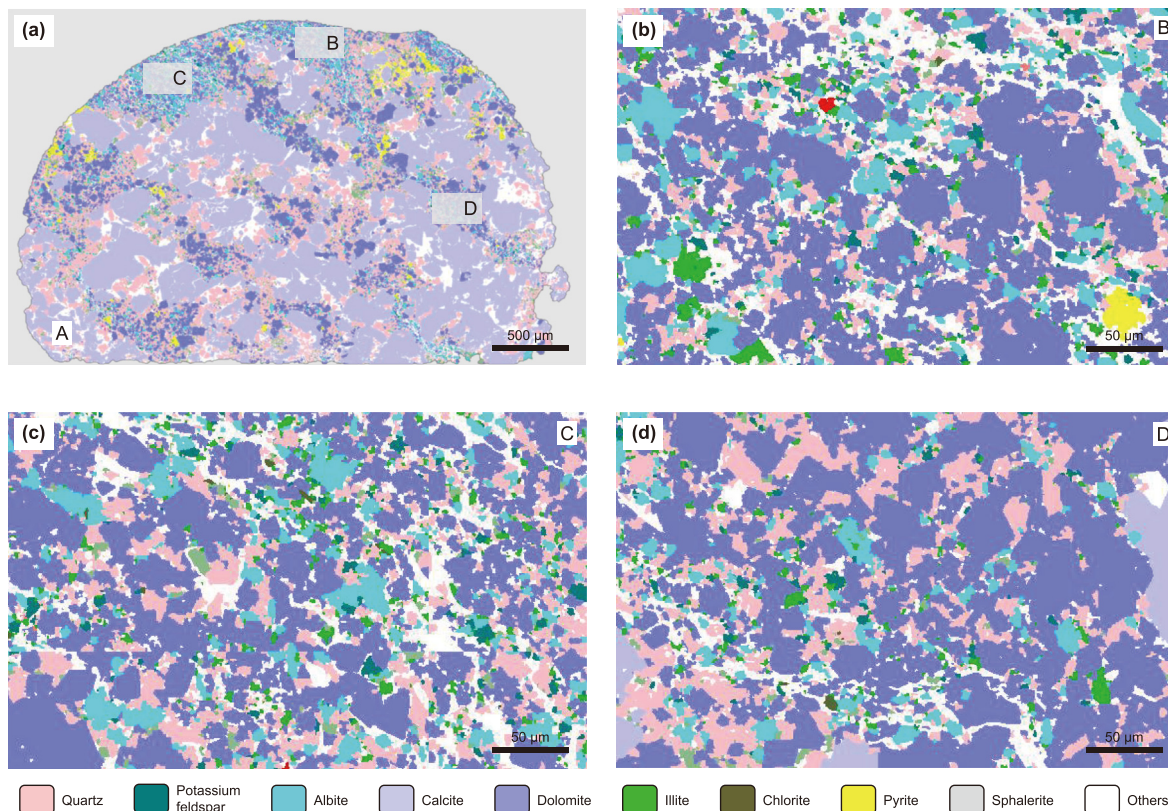


Fig. 9. The mineral composition of Sample 3-2. (a) The mineral composition mapping for the whole fractured section A; (b, c, d) The distributions of cracks and minerals in Region B, C, D.

Table 4
The area percentage of major minerals in different regions of Sample 3-2 (%).

	Region B	Region C	Region D
Dolomite	47.27	48.18	55.87
Albite	10.09	10.64	5.92
Quartz	18.98	13.62	20.80

and a length of 2101.61 μm, which connected two large pores (Fig. 10). Since this crack is rather thin, the mineral particles on either side are only slightly misaligned, without large chunks falling off. It is clear that during the development of the crack, some parts of it would go around the borders of different minerals, while other parts would go through the same mineral (Fig. 10(b)). The crack in Fig. 10(b) was not traced on purpose, to clearly show its morphology. In order to investigate the spatial relationship between minerals and the crack, the length rate of the crack extending around or through minerals is calculated (Table 5).

Among the four minerals, feldspar includes potassium feldspar and albite, and dolomite contains dolomite and ankerite. Because this sample contains abundant albite and dolomite, whose contents are 36.88% and 34.38% respectively, this crack predominantly develops within these two minerals, accounting for 83.85% of its total length, including 70.01% around the minerals and 13.84% through them. Apart from that, there are also 14.25% of crack develops around quartz. For the whole crack, 84.26% length propagates around the borders of different minerals, while only 15.74% develops through the same mineral. It is worth noticing that for minerals with higher Moh's hardness, such as quartz and feldspar, cracks are easier to develop around their borders; while for minerals with lower Moh's hardness, such as dolomite, cracks are

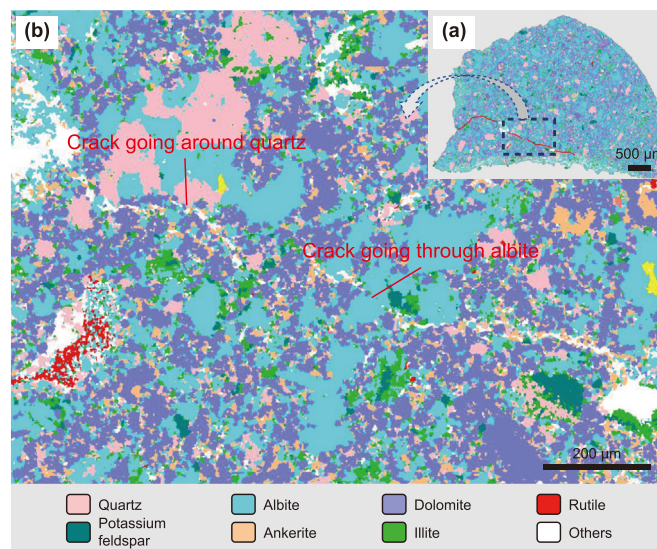


Fig. 10. The influence of minerals on fracture propagation in Sample 2-2. (a) The mineral composition mapping for the whole fractured section and the long thin crack developed here; (b) the spatial distribution between minerals and the crack.

relatively easier to develop through it, although the main way is still to bypass. In other words, as Moh's hardness increases, it becomes more difficult for the crack to develop through the mineral. This illustrates that the hardness of minerals is one of the reasons that influences the crack propagation.

Considering that the mechanical properties of rocks influenced

Table 5
The length rate of the crack extending around or through minerals.

Minerals	Moh's Hardness	Cracks Extending around/through Minerals	Rate of Length, %
Quartz	7	Around Through	14.25 –
Feldspar (Potassium feldspar and Albite)	6–6.5	Around Through	30.09 1.91
Dolomite (Dolomite and Ankerite)	3.5–4	Around Through	39.92 11.93
Clay	1–1.5	Through	1.91

by structural surfaces of various scales, the UCS of the small samples discussed in this article should only be thought as a reference and does not represent the UCS of standard-sized rock cores. While as for the fracture characteristics, since this article focuses on the influence of mineral composition and distribution on fracturing, rather than the influence of stress condition, in our opinion, the findings about the influences are basically general rules.

4. Conclusions

In this paper, the uniaxial compression test with real-time micro-CT scanning was conducted on shale layered samples from Lucaogou Formation, as well as the mineral analysis of fractured samples. This study reveals the difference of mechanical properties between the oil layer and interlayer, and the influence of mineral composition and distribution on micro-crack propagation. The following conclusions have been formed.

- (1) Based on the experimental studies on the samples in this work, compared with the interlayer samples, the surface porosity of oil-bearing samples is larger, with a lower uniaxial compressive strength and a higher elastic modulus.
- (2) The mineral composition and distribution affect the generation of micro-cracks. In this study, regions with one dominant mineral whose content is larger than 60% are prone to form a wide main crack after fracturing; while regions composed of 2–3 major minerals with a content of 10%–60% tend to form fractured zones consisting of many fine micro-cracks.
- (3) The hardness of minerals is also one of the reasons that influences the micro-crack propagation. As the Moh's hardness increases, it becomes more difficult for the crack to develop through the mineral.

CRedit authorship contribution statement

Xiu-Kuo Sun: Writing – review & editing, Writing – original draft, Visualization, Validation, Methodology, Investigation, Formal analysis, Data curation, Conceptualization. **Shou-Ding Li:** Supervision, Project administration, Funding acquisition, Conceptualization. **Xiao Li:** Supervision, Project administration, Funding acquisition. **Guan-Fang Li:** Writing – review & editing, Validation, Investigation. **Bo Zheng:** Writing – review & editing, Validation. **Tian-Qiao Mao:** Writing – review & editing, Validation. **Jing-Yun Guo:** Writing – review & editing.

Declaration of competing interest

The authors declare that they have no known competing financial interests or personal relationships that could have appeared to influence the work reported in this paper.

Acknowledgments

This work was supported by the National Natural Science Foundation of China (No. 42090023, 42102323, 51734009, 42102322), the Scientific Research and Technology Development Project of China National Petroleum Corporation (2022DJ5503), the Joint Geological Funds of the National Natural Science Foundation of China (U2244223).

References

- Chen, D., Pan, Z.J., Ye, Z.H., 2015. Dependence of gas shale fracture permeability on effective stress and reservoir pressure: model match and insights. *Fuel* 139, 383–392. <https://doi.org/10.1016/j.fuel.2014.09.018>.
- Crawford, B.R., Faulkner, D.R., Rutter, E.H., 2008. Strength, porosity, and permeability development during hydrostatic and shear loading of synthetic quartz-clay fault gouge. *J. Geophys. Res.-Sol. Ea* 113 (B3). <https://doi.org/10.1029/2006jB004634>.
- He, J.M., Li, X., Yin, C., Zhang, Y.X., Lin, C., 2020. Propagation and characterization of the micro cracks induced by hydraulic fracturing in shale. *Energy* 191, 116449. <https://doi.org/10.1016/j.energy.2019.116449>.
- Hu, T., Pang, X.Q., Jiang, S., Wang, Q.F., Zheng, X.W., Ding, X.G., Zhao, Y., Zhu, C.X., Li, H., 2018. Oil content evaluation of lacustrine organic-rich shale with strong heterogeneity: a case study of the Middle Permian Lucaogou Formation in Jimusaer Sag, Junggar Basin, NW China. *Fuel* 221, 196–205. <https://doi.org/10.1016/j.fuel.2018.02.082>.
- Kohli, A.H., Zoback, M.D., 2013. Frictional properties of shale reservoir rocks. *J. Geophys. Res.-Sol. Ea* 118 (9), 5109–5125. <https://doi.org/10.1002/jgrb.50346>.
- Kumar, V., Sondergeld, C.H., Rai, C.S., 2012. Nano to macro mechanical characterization of shale. In: SPE Annual Technical Conference and Exhibition, San Antonio, Texas, USA. <https://doi.org/10.2118/159804-MS>.
- Li, G.F., Jin, Z.J., Li, X., Liu, K.Q., Yang, W.C., Mao, T.Q., Zhou, T.T., Sun, X.K., 2023. Experimental study on mechanical properties and fracture characteristics of shale layered samples with different mineral components under cyclic loading. *Mar. Petrol. Geol.* 150, 106114. <https://doi.org/10.1016/j.marpetgeo.2023.106114>.
- Li, H., 2022. Research progress on evaluation methods and factors influencing shale brittleness: a review. *Energy Rep.* 8, 4344–4358. <https://doi.org/10.1016/j.egyrs.2022.03.120>.
- Li, J.M., Zou, Y.S., Shi, S.Z., Zhang, S.C., Wang, J.C., Ma, X.F., Zhang, X.H., 2022a. Experimental study on fracture propagation mechanism of shale oil reservoir of Lucaogou Formation in jimusaer. *Geofluids* 2022, 1–11. <https://doi.org/10.1155/2022/6598575>.
- Li, X., Duan, Y.T., Li, S.D., Zhou, R.Q., 2017. Study on the progressive failure characteristics of longmaxi shale under uniaxial compression conditions by X-ray micro-computed tomography. *Energies* 10 (3), 303. <https://doi.org/10.3390/en10030303>.
- Li, Y., Chen, J.Q., Elsworth, D., Pan, Z.J., Ma, X.T., 2022b. Nanoscale mechanical property variations concerning mineral composition and contact of marine shale. *Geosci. Front.* 13 (4), 101405. <https://doi.org/10.1016/j.gsf.2022.101405>.
- Li, Z.C., Li, L.C., Li, M., Zhang, L.Y., Zhang, Z.L., Huang, B., Tang, C.A., 2018. A numerical investigation on the effects of rock brittleness on the hydraulic fractures in the shale reservoir. *J. Nat. Gas Sci. Eng.* 50, 22–32. <https://doi.org/10.1016/j.jngse.2017.09.013>.
- Luo, Q.Y., Gong, L., Qu, Y.S., Zhang, K.H., Zhang, G.L., Wang, S.Z., 2018. The tight oil potential of the Lucaogou Formation from the southern Junggar Basin, China. *Fuel* 234, 858–871. <https://doi.org/10.1016/j.fuel.2018.07.002>.
- Miller, C.K., Waters, G.A., Rylander, E.I., 2011. Evaluation of production log Data from horizontal wells drilled in organic shales. In: North American Unconventional Gas Conference and Exhibition. <https://doi.org/10.2118/144326-MS>.
- Revil, A., Grauls, D., Brévar, O., 2002. Mechanical compaction of sand/clay mixtures. *J. Geophys. Res.-Sol. Ea* 107 (B11), 2293. <https://doi.org/10.1029/2001JB000318>.
- Sone, H., Zoback, M.D., 2013. Mechanical properties of shale-gas reservoir rocks — Part 1: static and dynamic elastic properties and anisotropy. *Geophysics* 78 (5), D381–D392. <https://doi.org/10.1190/geo2013-0050.1>.
- Sun, X.K., Li, S.D., Li, X., Li, G.F., Zheng, B., Mao, T.Q., 2023. The mechanical properties

- and fracture characteristics of shale layered samples from the Lucaogou Formation considering natural crack and mineral distribution. *Materials* 16 (17), 5881. <https://doi.org/10.3390/ma16175881>.
- Sun, X.K., Li, X., Mao, T.Q., Zheng, B., Wu, Y.F., Li, G.F., 2021. Fracture evolution analysis of soil-rock mixture in contrast with soil by CT scanning under uniaxial compressive conditions. *Sci. China Technol. Sc.* 64 (12), 2771–2780. <https://doi.org/10.1007/s11431-020-1888-9>.
- Sun, X.K., Li, X., Zheng, B., He, J.M., Mao, T.Q., 2020. Study on the progressive fracturing in soil and rock mixture under uniaxial compression conditions by CT scanning. *Eng. Geol.* 279, 105884. <https://doi.org/10.1016/j.enggeo.2020.105884>.
- Tulu, I.B., 2009. *Modeling PDC Cutter Rock interaction*. West Virginia University.
- Wang, Y., Li, X., Zhang, B., Zhao, Z.H., 2016. Optimization of multiple hydraulically fractured factors to maximize the stimulated reservoir volume in silty laminated shale formation, Southeastern Ordos basin, China. *J. Petrol. Sci. Eng.* 145, 370–381. <https://doi.org/10.1016/j.petrol.2016.05.033>.
- Wu, S.T., Zhai, X.F., Yang, Z., Bale, H., Hong, Y.L., Cui, J.W., Pan, S.Q., Lin, S.H., 2019. Characterization of fracture formation in organic-rich shales— an experimental and real time study of the Permian Lucaogou Formation, Junggar Basin, northwestern China. *Mar. Petrol. Geol.* 107, 397–406. <https://doi.org/10.1016/j.marpetgeo.2019.05.036>.
- Xu, Y., Lun, Z.M., Pan, Z.M., Wang, H.T., Zhou, X., Zhao, C.P., Zhang, D.F., 2022. Occurrence space and state of shale oil: a review. *J. Petrol. Sci. Eng.* 211, 110183. <https://doi.org/10.1016/j.petrol.2022.110183>.
- Yang, C., Xiong, Y.Q., Wang, J.F., Li, Y., Jiang, W.M., 2020. Mechanical characterization of shale matrix minerals using phase-positioned nanoindentation and nano-dynamic mechanical analysis. *Int. J. Coal Geol.* 229, 103571. <https://doi.org/10.1016/j.coal.2020.103571>.
- Zhang, X.H., Zhang, S.C., Zou, Y.S., Li, J.M., Wang, J.C., Zhu, D.Y., Zhou, G.J., Yang, C., 2022. Effect of Interlaminar difference on height propagation behavior of hydraulic fracture in Lucaogou shale. In: *The 56th U.S. Rock Mechanics/Geomechanics Symposium*, Santa Fe, New Mexico, USA: ARMA-2022-0969. <https://doi.org/10.56952/ARMA-2022-0969>.
- Zhang, Y.F., Niu, S.Y., Du, Z.M., Hao, J., Yang, J.J., 2020. Dynamic fracture evolution of tight sandstone under uniaxial compression in high resolution 3D X-ray microscopy. *J. Petrol. Sci. Eng.* 195, 107585. <https://doi.org/10.1016/j.petrol.2020.107585>.
- Zhou, M.Y., Zhang, Y.F., Zhou, R.Q., Hao, J., Yang, J.J., 2018. Mechanical property measurements and fracture propagation analysis of longmaxi shale by micro-CT uniaxial compression. *Energies* 11 (6), 1409. <https://doi.org/10.3390/en11061409>.
- Zoback, M.D., Moos, D., Mastin, L., Anderson, R.N., 1985. Wellbore breakouts and in situ stress. *J. Geophys. Res.* 90 (B7), 5523–5530.
- Zou, C.N., Yang, Z., Cui, J.W., Zhu, R.K., Hou, L.H., Tao, S.Z., Yuan, X.J., Wu, S.T., Lin, S.H., Wang, L., Bai, B., Yao, J.L., 2013. Formation mechanism, geological characteristics and development strategy of nonmarine shale oil in China. *Petrol Explor Dev.* 40 (1), 15–27. [https://doi.org/10.1016/S1876-3804\(13\)60002-6](https://doi.org/10.1016/S1876-3804(13)60002-6).
- Zou, C.N., Yang, Z., Tao, S.Z., Li, W., Wu, S.T., Hou, L.H., Zhu, R.K., Yuan, X.J., Wang, L., Gao, X.H., Jia, J.H., Guo, Q.L., 2012. Nano-hydrocarbon and the accumulation in coexisting source and reservoir. *Petrol Explor Dev.* 39 (1), 15–32. [https://doi.org/10.1016/S1876-3804\(12\)60011-1](https://doi.org/10.1016/S1876-3804(12)60011-1).